Journal of Power Sources 414 (2019) 272–277

Contents lists available at ScienceDirect

Journal of Power Sources

journal homepage: www.elsevier.com/locate/jpowsour

Short communication

Investigation of water generation and accumulation in polymer electrolyte fuel cells using hydro-electrochemical impedance imaging

Y. Wu[a], Q. Meyer[b], F. Liu[c], L. Rasha[a], J.I.S. Cho[a], T.P. Neville[a], J. Millichamp[a], R. Ziesche[a], N. Kardjilov[d], P. Boillat[e], H. Markötter[d], I. Manke[d], M. Cochet[e], P. Shearing[a,*], D.J.L. Brett[a,**]

[a] Electrochemical Innovation Lab, Department of Chemical Engineering, University College London, London, WC1E 7JE, United Kingdom
[b] Nanoelectrochemistry Group, School of Chemistry, UNSW, Sydney, 2052, Australia
[c] Department of Electronic & Electrical Engineering, University College London, London, WC1E 7JE, United Kingdom
[d] Helmholtz-Zentrum Berlin (HZB), Hahn-Meitner-Platz 1, 14109, Berlin, Germany
[e] Neutron Imaging and Activation Group (NIAG), Paul Scherrer Institut (PSI), CH-5232, Villigen, Switzerland

HIGHLIGHTS

- Hydro-electrochemical impedance imaging applied to water management of PEFC.
- HECII distinguish between 'legacy' and 'nascent' water in the PEFC.
- The perturbation frequency of HECII affects water dynamics features.

ARTICLE INFO

Keywords:
Neutron imaging
Polymer electrolyte fuel cell
Water management
Electro-hydrography

ABSTRACT

In-depth understanding of water management is essential for the optimization of the performance and durability of polymer electrolyte fuel cells (PEFCs). Neutron imaging of liquid water has proven to be a powerful diagnostic technique, but it cannot distinguish between 'legacy' water that has accumulated in the system over time and 'nascent' water recently generated by reaction. Here, a novel technique is introduced to investigate the spatially resolved water exchange characteristics inside PEFCs. Hydro-electrochemical impedance imaging (HECII) involves making a small AC-sinusoidal perturbation to a cell and measuring the consequential water generated, using neutron radiographs, associated with the stimulus frequency. Subsequently, a least-squares estimation (LSE) analysis is applied to derive the spatial amplitude ratio and phase shift. This technique provides a complementary view to conventional neutron imaging and provides information on the source and 'history' of water in the system. By selecting a suitable perturbation frequency, HECII can be used to achieve an alternative image 'contrast' and identify different features involved in the water dynamics of operational fuel cells.

1. Introduction

Polymer electrolyte fuel cells (PEFCs) operating on hydrogen are a potential solution to the increasing demand for sustainable energy conversion technologies. They have demonstrated significant advances in terms of performance, efficiency and durability for a wide range of applications. However, there is scope for further improvements. One of the long-standing challenges to ensuring efficient and reliable PEFC performance is accomplishing effective internal water management [1–3]. Having access to bespoke in-situ diagnostic techniques capable of studying internal water dynamics is key to optimizing components and operating conditions.

Neutron radiography is arguably the most powerful method for visualization and quantification of the water distribution in operating PEFCs [4–11]. This technique satisfies three requirements defined by Stumper et al. [12]: (i) in-situ applicability, (ii) minimal invasiveness and (iii) ability to provide information on the distribution of liquid water over the active area. It offers several advantages over other visualization techniques, such as optical visualization and X-ray radiography, including high sensitivity to water, and minimal requirement for modification to the design and material of cell components (*i.e.,* no need for an optical window) [4]. This technique can capture 'absolute'

* Corresponding author.
** Corresponding author.
E-mail addresses: p.shearing@ucl.ac.uk (P. Shearing), d.brett@ucl.ac.uk (D.J.L. Brett).

https://doi.org/10.1016/j.jpowsour.2019.01.003
Received 17 October 2018; Received in revised form 21 December 2018; Accepted 3 January 2019
0378-7753/

water content thickness with high spatial resolution, but lacks the ability to distinguish between 'legacy' water (quiescent water that has accumulated and remained in the system for an extended period – it may coalesce or get redistributed over time) and 'fresh' or 'nascent' water recently generated by the electrochemical reaction. Identification of areas prone to appear 'nascent' water is indispensable for optimization of performance and durability of PEFCs. The propensity to flooding in such areas is possibly due to the local hydrophilic/phobic nature of GDLs/flow-fields and/or non-uniform compression across the active area. This can lead to local reactant starvation and mechanical stress in the membrane electrode assembly (MEA), these can be detrimental to fuel cell performance and longevity [13]. To address this issue, hydrogen-deuterium contrast neutron radiography had been developed which enables quantification of the local water exchange rate inside PEFCs [14]. However, this technique entails certain drawbacks such as high cost and operational complexity.

Electrochemical impedance spectroscopy (EIS) is a well-established characterization technique that has been extensively used in the study of PEFCs [15]. This technique can distinguish and separate the different loss mechanisms of a PEFC, such as charge transfer, ohmic and mass transport resistance, providing selective information about the operation of the electrodes and electrolyte [16–20]. This is a form of transfer function analysis, which allows processes occurring with different time constants to be identified by analyzing the cause/effect relationship between a sinusoidal perturbation to a system and its consequence. In EIS, this is the relationship between current and voltage. Novel transfer function diagnostic techniques have been applied to PEFC, such as electrochemical thermal impedance spectroscopy (ETIS), which uses the relationship between current perturbation (load on the fuel cell) and the consequent temperature change, to map PEFC operation [21]. The relationship between the sinusoidal perturbation of reactant pressure and cell voltage response (electrochemical pressure impedance spectroscopy - EPIS) has been used to gain deeper insight into the mass transfer effects in PEFCs [22]. Here, the transfer function approach is extended to consider the relationship between current and spatial water generation/evaporation using neutron imaging in so-called hydro-electrochemical impedance imaging (HECII). Heterogeneous local current density distribution and flow-field channel configuration (land/channel) result in spatially variant water exchange characteristics. This technique is complementary to conventional water distribution neutron imaging in that it uses a different 'lens' to examine water dynamics explicitly associated with water exchange/transport/generation occurring on the time-scale of the current perturbation, as opposed to the simple existence of water in the system.

In this work, the response of the localized water thickness to an AC-current perturbation is recorded using neutron imaging. Using the well-established least-squares estimation (LSE) method, the relative amplitude ratio and phase shift between the periodic current stimulus and the water response has been derived at different frequencies to decouple processes with different time constants.

2. Experimental

2.1. Fuel cell design

A closed-cathode PEFC with an active area of 25 cm^2 was designed for testing. The cell consisted of two aluminium current collectors, two graphite flow-fields (Schunk, Germany), a MEA, gaskets and two end-plates (Fig. 1 (a)). A horizontal five-channel serpentine geometry was used for the cathode flow-field, and a vertical single channel serpentine was used for the anode (Fig. 1 (b)). The width of land and channel, and the depth of the channel, were all equal to 1 mm. The anode and cathode gases were fed in cross-flow orientation. A 70 μm thick sheet of Tygaflor was used as gasket at the interface between the flow-fields/current collectors and end-plates for electrical insulation. A Tygaflor sheet was used as the gasket to seal the perimeter of the MEA. The two current collectors and the anode end-plate were electroless gold plated to prevent corrosion.

The MEA was fabricated in-house by hot pressing Nafion 212 membrane (DuPont, USA) and ELE00162 Johnson Matthey gas diffusion electrodes (GDL coated with catalyst layer 0.4 mg Pt cm^{-2} at both sides). The MEA was pressed at 130 °C for 3 min with an applied pressure of 400 psi [23]. The GDL contains a micro porous layer (MPL) for enhanced performance of the GDL catalyst layer interface.

2.2. Fuel cell testing

In-house designed test station and control software (LabVIEW, National Instruments, USA) were used to operate the PEFC (air, hydrogen, and the load) and record the data with a data acquisition card (DAQ card, USB 6363, National Instruments, USA). The PEFC was operated at ambient temperature in the absence of gas humidification. The stoichiometry of cathode and anode flow were 2 and 1.2 respectively. The flow rates of gas inlets were controlled using two calibrated digital mass flow controllers (Bronkhorst, UK). Current was drawn from the fuel cell using a DC electronic load (PLZ664WA, Kikusui) and the 20 mA cm^{-2} peak amplitude AC perturbation was applied to the system on top of a 200 mA cm^{-2} DC offset.

2.3. Neutron imaging

The cold neutron radiography (CONRAD) beamline at Helmholtz-Zentrum Berlin (HZB) was employed for the experiments. The beam is formed by a neutron guide and an additional collimation system, consisting of a 3 cm pinhole at a distance of 5 m, resulting in an L/D ratio of 167. Subsequently, the beam is transmitted through the PEFC. The detector consists of an sCMOS camera (Andor Neo) facing a 200 μm LiF/ZnS neutron scintillator screen. The neutron scintillator converts neutrons into visible light, which is then detected by the camera. The cell was placed in through-plane orientation to the beam to visualize liquid water across the entire active area. An imaging field-of-view of (56 × 67) mm^2 with a pixel size of 26 μm was achieved using the imaging set-up developed by Kardjilov et al. [24]. Each image was taken with an exposure time of 5 s.

To distinguish liquid water from the rest of the PEFC components, images taken during cell operation were normalised to a dry fuel cell image taken at the beginning of each experiment. The total water thickness of each image δ_{water}, was calculated through the following equation by inverting the Beer-Lambert law:

$$\delta_{water} = -\frac{\ln(I/I_0)}{\varepsilon_{water}} \quad (1)$$

Where ε_{water} refers to the attenuation coefficient of neutrons in liquid water; measured with the given neutron spectrum at 5.3 cm^{-1}, and I_0 is the intensity of the reference image (without water), which was taken after the dry gas was flowing through both sides of the cell for 10 min before each experiment. I refers to the intensity of the 'working' image, which was taken during the cell was in operation.

2.4. Calculation of the amplitude ratio and phase-shift

The dynamics of liquid water (generation/evaporation or triggered by the gas flow) is evaluated using the amplitude ratio and phase shift between the periodic current stimulus and the water thickness response. A small sinusoidal current perturbation was applied to the cell, and the water thickness variation across the active area was recorded by a series of neutron radiographs as the response signal.

The sinusoidal current density perturbation was generated using LabVIEW (National Instruments) as follows.

$$i(t, f) = i_{ac} \sin(2\pi ft) + i_{dc} \quad (2)$$

Here, i is current density, i_{ac} is the peak amplitude of the current

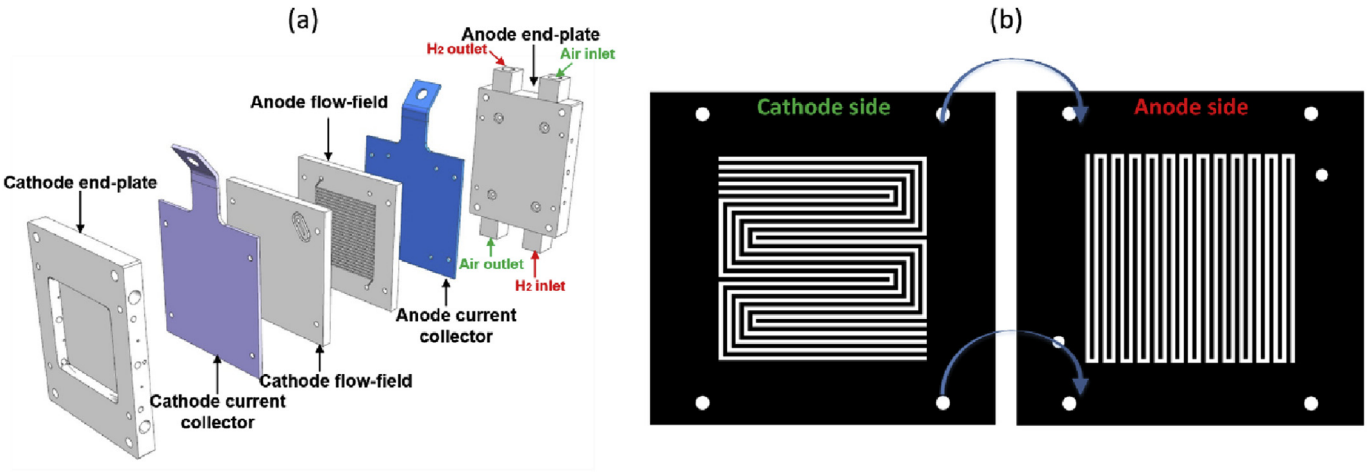

Fig. 1. (a) Exploded view of individual PEFC components (excluding the MEA, which is between the flow-field plates); (b) flow-field design. For assembling, the cathode side is placed over the anode side.

perturbation (20 mA cm^{-2}), i_{dc} is the DC offset of current density (200 mA cm^{-2}), f is frequency and t is time.

It was assumed the theoretical water thickness response $W_{theo}(n)$ is the standard sinusoidal signal at each pixel:

$$W_{theo}(n) = A_{i,W}\sin(2\pi fn + \phi_{i,W}) + D_{i,W}, \quad n = 0,1, \ldots, N-1, \tag{3}$$

Where $A_{i,W}$ is the peak amplitude of response signal (water thickness), $\phi_{i,W}$ is the phase shift and $D_{i,W}$ is the water thickness offset.

The neutron images show that the water thickness response (Fig. 2) is at the same frequency as the imposed current perturbation but out of phase. To account for experimental noise in the system, additive white Gaussian noise (AWGN) is assumed to operate on the theoretical data $W_{theo}(n)$. The Gaussian assumption is a reasonable approximation when the actual probability distribution of the experimental noise remains unknown. As per the central limit theorem (CLT) [25], when independent random variables are added, their sum tends toward a Gaussian distribution even if the original variables themselves are not Gaussian distributed. Therefore, we consider the local water thickness (response signal) $W_{known}(n)$ comprises two parts: the theoretical water thickness response $W_{theo}(n)$ and the AWGN$w(n)$:

$$W_{known}(n) = W_{theo}(n) + w(n), \quad n = 0,1, \ldots, N-1, \tag{4}$$

A sinusoidal fit was applied to the current perturbation $i(t, f)$ and the water thickness response $W_{known}(n)$ to determine the set of $A_{i,W}$, $\phi_{i,W}$ and $D_{i,W}$. The requirement of this fit is to minimize the sum of the residuals between $W_{known}(n)$ and $W_{theo}(n)$ at each pixel across the active area. The maximum likelihood estimation (MLE) is the most effective method for the given classic linear model. By the AWGN assumption, this is equivalent to finding the nearest (in a Euclidean norm sense) sinusoid signal as the approximation, which is the so-called least-squares estimation (LSE) [26]. The detailed calculation of $A_{i,W}$, $\phi_{i,W}$ and $D_{i,W}$ is shown in the Supplementary Material. Subsequently, the amplitude ratio (AR, absolute term) at each pixel can be evaluated as the relative peak amplitude of the water thickness response ($A_{i,W}$) and current perturbation (i_{ac}) during two complete cycles (0–2000 s):

$$AR(\mu mmA^{-1}) = \frac{A_{i,W}}{i_{ac}} \tag{5}$$

The phase shift is the time lag between the water thickness response and current perturbation.

$$\phi(\text{degree}) = \phi_{i,W}\frac{180}{\pi} \tag{6}$$

The AR demonstrates the extent to which water is generated/removed during the cycle period. The phase shift reveals temporal information, highlighting that different parts of the cell have different water generation/removal dynamics. Areas with the most rapid response having a phase closest to zero degrees.

The spatially resolved R-squared during two complete cycles (0–2000 s) has been provided (Supplementary Material) to validate the effectiveness of HECII. R-squared denotes the coefficient of determination, which is a goodness-of-fit measure [27]. An R-squared threshold value of 0.6 has been applied to the 'raw' image (Fig. S1 (a)) with the amplitude ratio of the pixels that do not fit the criteria set to 0.

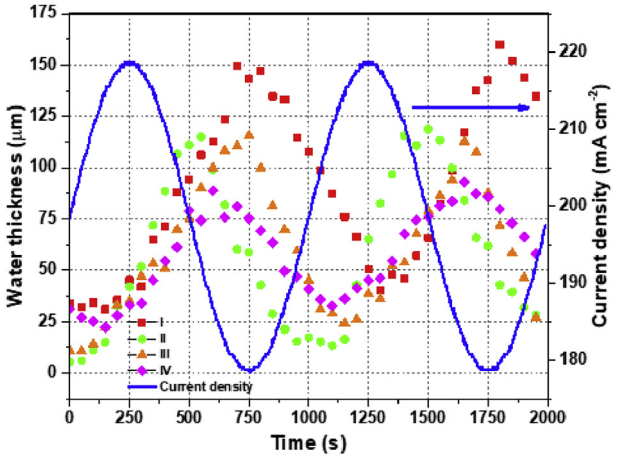

Fig. 2. Temporal data of current stimulus (blue) plotted with the water thickness response at four different locations across the active cell area (Fig. 3). (For interpretation of the references to colour in this figure legend, the reader is referred to the Web version of this article.)

3. Results and discussion

The system was operated at 200 mA cm^{-2} and perturbed with a 20 mA cm^{-2} peak amplitude current stimulus at 1 mHz over 2 periods (Fig. 2). The time-domain water response from neutron images at different locations on the PEFC (Fig. 3(b)) has a sinusoidal behavior (Fig. 2). The sinusoidal current perturbation elicits a clear, periodic water response at different locations of the cell. There is a time-lag (phase shift) between the current perturbation and the water thickness response and variation in amplitude that varies with location across the electrode area.

A radiograph of the dry cell (Fig. 3 (a)) highlights the cell structure and the gas feeding/flow direction. A complete image series during current density perturbation over 2 periods (0–2000 s) is taken into

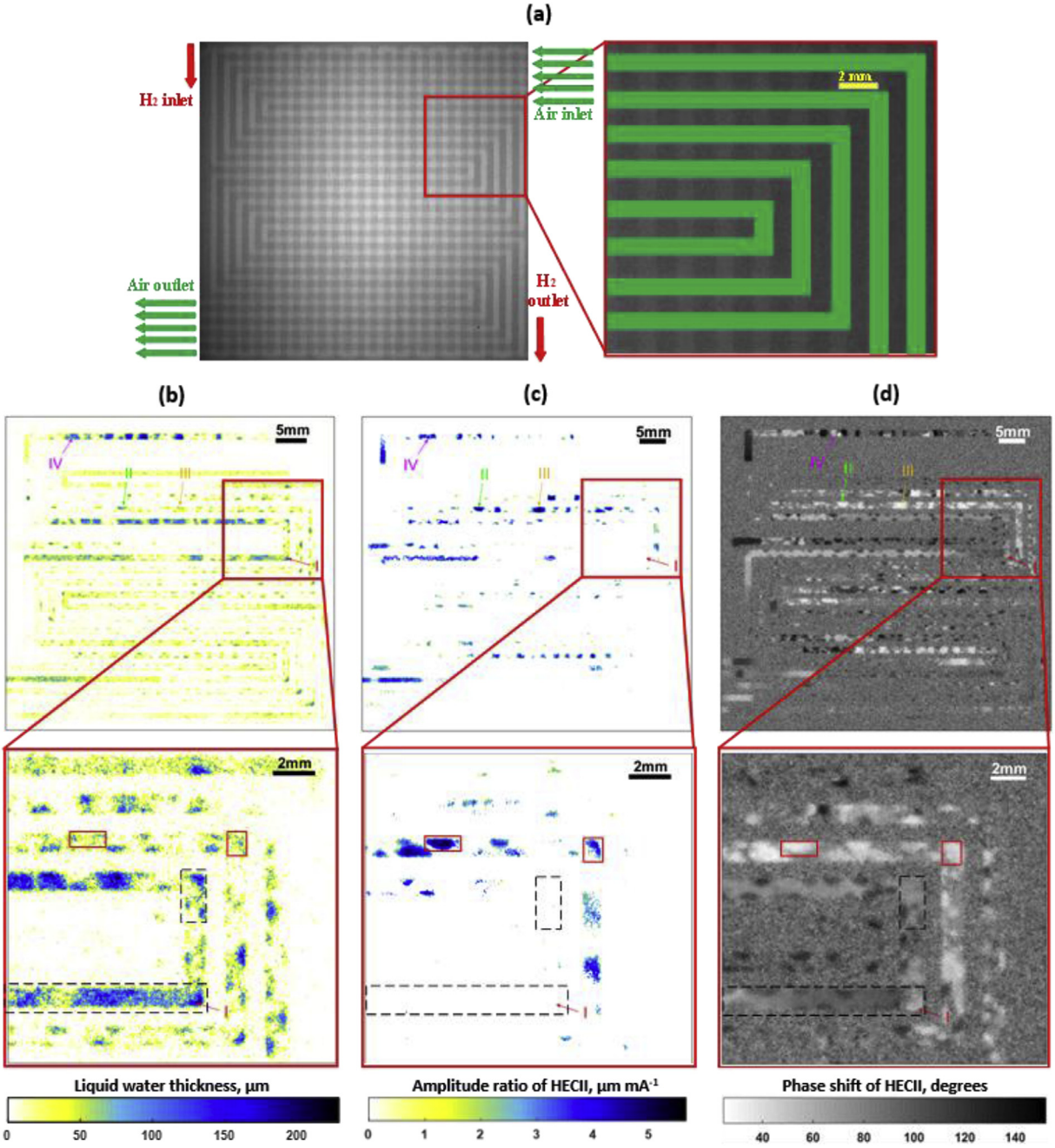

Fig. 3. (a) Radiograph of the dry cell (the cathode channels in the magnified view are masked in green. (b) Averaged liquid water thickness distribution, (c) HECII amplitude ratio and (d) HECII phase shift over the same period as Fig. 2 (0–2000 s). The whole active cell area (top), with a magnified cut-out of the selected local area highlighted in solid red squares (bottom). (For interpretation of the references to colour in this figure legend, the reader is referred to the Web version of this article.)

account. The conventional neutron radiograph of averaged water distribution (Fig. 3 (b)) is compared with the amplitude ratio and phase shift of the HECII (Fig. 3(c) and (d)). The neutron radiographs (grey scale) were coloured with a yellow/blue mask as a guide for the eye (where blue indicates highest liquid water). The horizontal five-channel serpentine geometry of the cathode and vertical single-channel serpentine at the anode (Fig. 1 (b)) makes it possible to distinguish which electrode the water belongs to. Liquid water is mainly found at the cathode (horizontal channels) with water accumulation occurring primarily in the open channel areas and some water transported to the anode via the back-diffusion [5,8,28].

It is noted that liquid water accumulates on the side-wall of the flow channel (such as region 'II', 'III' and 'IV' in Figs. 3 (b), 105–155 µm), as has been reported in other neutron imaging studies [29–32]. One explanation is that the lands are cooler than at the open channel/GDL interface [33,34]. Consequently, water vapour preferentially condenses under the land and liquid water starts 'bulging' into the channel once the region under the land is saturated. Liquid water also tends to accumulate around channel bends, as can be observed in region 'I' ((Fig. 3 (b) between 150 and 205 µm). This is a well-known feature in serpentine flow-fields [35–37], and is attributed to the decreasing channel-to-channel pressure gradient near the bend and/or disturbance of the gas flow as it traverses a corner region.

The dashed black boxes in the magnified cut-out (Fig. 3 (b)) highlights water agglomerates, where nearly half of the channel width is filled with liquid water (115–200 µm). However, the HECII in the same

region (Fig. 3 (c)) does not register a significant amplitude ratio. This implies that this is legacy water that has accumulated in the channels and not nascent water generated from recent reaction (locked-in to the current stimulus). On the other hand, the solid red boxes in the magnified cut-out of Fig. 3(b) and (c) reveal locations with a high amplitude ratio (3.5–5.2 μm mA^{-1}) but a lower water accumulation (55–84 μm) in the conventional neutron radiograph, indicating that this is associated with the current perturbation and therefore a result of recent water generation.

This is partly due to the fact that water slugs or droplet flow along the channels is unlikely to be sinusoidal, as water detachment from the flow channel edges and movement is likely to be random [7,8]. Neither 'legacy' water nor water slugs/droplets triggered by the gas flow will be affected by the sinusoidal current perturbation and therefore undetected on the R-squared image (as seen in the paragraph after Fig. S1). Subsequently, they will not appear in the 'filtered' amplitude-ratio of HECII after adding R-squared threshold (Fig. S1 (c)). On the other hand, the 'nascent' water is instantly renewed by the current perturbation, which is highlighted via this technique.

The phase shift provides an indication of the relative temporal emergence of water associated with the current perturbation cycle and adds a different 'contrast' with which to examine water distribution. For example, the phase shift in the solid red boxes (30–45°) is much lower than in the dashed black boxes (65–110°), indicating a faster response to the current perturbation in the former region. The temporal water dynamics are clearly complex. Variation in the rate of water accumulation and removal could be due to factors such as: varying flow characteristics in different channels and parts of channels; heterogeneous current generation across the electrodes; temperature variation; different GDL compression and variation in MEA properties, etc.

To study the influence of the stimulation frequency on the HECII response, it was varied over an order of magnitude (5 mHz, 1 mHz and 0.5 mHz). These frequencies were selected based on the typical time scale of water increasing from one steady-state to another, as determined by conventional radiography for this cell (~100 s - 2500 s) and also representative of that reported in the literature [29,38–40].

The system was operated at 200 mA cm^{-2} and perturbed with a 20 mA cm^{-2} peak amplitude current stimulus at different frequencies over 2 periods. The corresponding amplitude-ratio of the HECII over the current perturbation is shown in Fig. 4(a–c). At the highest frequency (5 mHz, 0–400 s), hardly any features are discernible, increasing in image richness as the frequency decreases. The longer cycle period allows more water to be accumulated. This implies that different cell geometries and operating conditions (i.e., current density, flow rate, temperature) will have different water dynamic rate constants that can be probed using different perturbation frequencies, in much the same way as conventional EIS, only as an image.

This technique is designed to derive the amplitude-ratio and phase-shift of the HECII over the complete current perturbation, rather than the instantaneous water generation and accumulation information. As for the fast movement of droplets/slugs, this could potentially be captured by increasing the frequency rate (using ultra-fast neutron imaging) to improve accuracy and track individual water movement, this will be the subject of future work.

4. Conclusions

A novel transfer function based neutron imaging technique, hydro-electrochemical impedance imaging (HECII) has been introduced and applied to provide new insight into the water management of PEFCs. In this method, a small current perturbation is applied to the cell, and the water thickness variation across the active area is recorded by a series of neutron radiographs as the response signal. Subsequently, a least-squares estimation (LSE) analysis is applied to derive the spatially-resolved HECII amplitude ratio and phase shift. The results reveal that the distribution of the phase shift and amplitude ratio is highly inhomogeneous within the cell. By selecting a suitable perturbation frequency, HECII can generate an image contrast and identify different features of local water exchange characteristics. The application of HECII provides a complementary view to that of conventional neutron imaging in that it highlights the location of nascent water generation.

Acknowledgements

The authors would like to acknowledge the financial support from China Scholarship Council and a UCL Faculty of Engineering Sciences Dean's Scholarship for Wu Yunsong. The authors would also like to acknowledge the EPSRC for supporting the Electrochemical Innovation Lab through (EP/M009394/1, EP/G030995/1, EP/I037024/1, EP/M014371/1 and EP/M023508/1). The authors gratefully acknowledge the financial support from an EPSRC "Frontier Engineering" Award (EP/K038656/1) and a UCL Faculty of Engineering Sciences Dean's Scholarship for Jason I. S. Cho. The authors would also like to acknowledge the financial support from the STFC/MDC Futures Early Career Award (ST/N002385/1) for L. Rasha.

Appendix A. Supplementary data

Supplementary data to this article can be found online at https://doi.org/10.1016/j.jpowsour.2019.01.003.

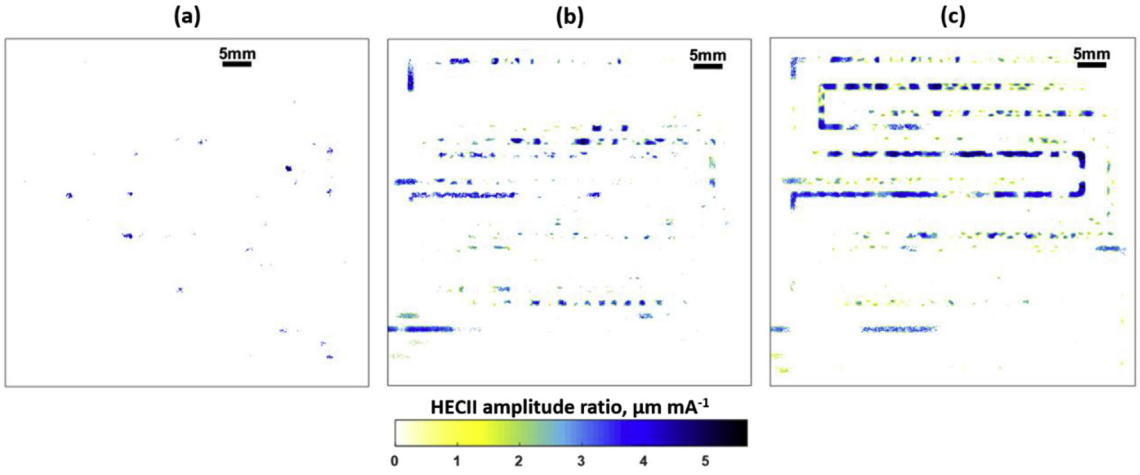

Fig. 4. Amplitude ratio of HECII over two current perturbation cycles at (a) 5 mHz, 0–400 s (b) 1 mHz, 0–2000 s and (c) 0.5 mHz, 0–4000 s.

References

[1] I. Tolj, D. Bezmalinovic, F. Barbir, Maintaining desired level of relative humidity throughout a fuel cell with spatially variable heat removal rates, Int. J. Hydrogen Energy 36 (20) (2011) 13105–13113.

[2] J.P. Owejan, J.J. Gagliardo, J.M. Sergi, S.G. Kandlikar, T.A. Trabold, Water management studies in PEM fuel cells, Part I: fuel cell design and in situ water distributions, Int. J. Hydrogen Energy 34 (8) (2009) 3436–3444.

[3] M. Ji, Z. Wei, A review of water management in polymer electrolyte membrane fuel cells, Energies 2 (4) (2009) 1057–1106.

[4] A. Bazylak, Liquid water visualization in PEM fuel cells: a review, Int. J. Hydrogen Energy 34 (9) (2009) 3845–3857 2009.

[5] Q. Meyer, S. Ashton, R. Jervis, D.P. Finegan, P. Boillat, M. Cochet, O. Curnick, T. Reisch, P. Adcock, P.R. Shearing, D.J. Brett, The hydro-electro-thermal performance of air-cooled, open-cathode polymer electrolyte fuel cells: combined localised current density, temperature and water mapping, Electrochim. Acta 180 (2015) 307–315.

[6] R. Anderson, L. Zhang, Y. Ding, M. Blanco, X. Bi, D.P. Wilkinson, A critical review of two-phase flow in gas flow channels of proton exchange membrane fuel cells, J. Power Sources 195 (15) (2010) 4531–4553.

[7] Y. Wu, J.I.S. Cho, X. Lu, L. Rasha, T.P. Neville, J. Millichamp, R. Ziesche, N. Kardjilov, H. Markötter, P.R. Shearing, D.J.L. Brett, Effect of compression on the water management of polymer electrolyte fuel cells: an in-operando neutron radiography study, J. Power Sources 412 (2019) 597–605.

[8] Y. Wu, J.I.S. Cho, T.P. Neville, Q. Meyer, R. Ziesche, P. Boillat, M. Cochet, P.R. Shearing, D.J.L. Brett, Effect of serpentine flow-field design on the water management of polymer electrolyte fuel cells: an in-operando neutron radiography study, J. Power Sources 399 (2018) 254–263.

[9] P. Boillat, E.H. Lehmann, P. Trtik, M. Cochet, Neutron imaging of fuel cells–Recent trends and future prospects, Curr. Opin. Electrochem. 5 (1) (2017) 3–10.

[10] R. Satija, D.L. Jacobson, M. Arif, S.A. Werner, In situ neutron imaging technique for evaluation of water management systems in operating PEM fuel cells, J. Power Sources 129 (2) (2004) 238–245.

[11] P. Boillat, A. Iranzo, J. Biesdorf, Layer by layer segmentation of water distribution from neutron imaging of large scale cells, J. Electrochem. Soc. 162 (6) (2015) F531–F536.

[12] J. Stumper, M. Löhr, S. Hamada, Diagnostic tools for liquid water in PEM fuel cells, J. Power Sources 143 (2005) 150–157.

[13] P. Trogadas, J.I.S. Cho, T.P. Neville, J. Marquis, B. Wu, D.J.L. Brett, M.O. Coppens, A lung-inspired approach to scalable and robust fuel cell design, Energy Environ. Sci. 11.1 (2018) 136–143.

[14] I. Manke, C. Hartnig, N. Kardjilov, M. Messerschmidt, A. Hilger, M. Strobl, W. Lehnert, J. Banhart, Characterization of water exchange and two-phase flow in porous gas diffusion materials by hydrogen-deuterium contrast neutron radiography, Appl. Phys. Lett. 92 (24) (2008) 244101.

[15] H. Wang, X.Z. Yuan, H. Li (Eds.), PEM Fuel Cell Diagnostic Tools, vol. 2, CRC press, 2011.

[16] J.M. Le Canut, R.M. Abouatallah, D.A. Harrington Harrington, Detection of membrane drying, fuel cell flooding, and anode catalyst poisoning on PEMFC stacks by electrochemical impedance spectroscopy, J. Electrochem. Soc. 153 (5) (2006) A857–A864.

[17] J.O. Schumacher, P. Gemmar, M. Denne, M. Zedda, M. Stueber, Control of miniature proton exchange membrane fuel cells based on fuzzy logic, J. Power Sources 129 (2) (2004) 143–151.

[18] M. Ciureanu, Effects of Nafion® dehydration in PEM fuel cells, J. Appl. Electrochem. 34 (7) (2004) 705–714.

[19] N. Wagner, E. Gülzow, Change of electrochemical impedance spectra (EIS) with time during CO-poisoning of the Pt-anode in a membrane fuel cell, J. Power Sources 127 (1) (2004) 341–347.

[20] M.A. Rubio, A. Urquia, S. Dormido, Diagnosis of performance degradation phenomena in PEM fuel cells, Int. J. Hydrogen Energy 35 (7) (2010) 2586–2590.

[21] E. Engebretsen, J.B. Robinson, O. Obeisun, T. Mason, D. Finegan, G. Hinds, P.R. Shearing, D.J. Brett, Electro-thermal impedance spectroscopy applied to an open-cathode polymer electrolyte fuel cell, J. Power Sources 302 (2016) 210–214.

[22] E. Engebretsen, T.J. Mason, P.R. Shearing, G. Hinds, D.J. Brett, Electrochemical pressure impedance spectroscopy applied to the study of polymer electrolyte fuel cells, Electrochem. Commun. 75 (2017) 60–63.

[23] Q. Meyer, N. Mansor, F. Iacoviello, P.L. Cullen, R. Jervis, D. Finegan, C. Tan, J. Bailey, P.R. Shearing, D.J.L. Brett, Investigation of hot pressed polymer electrolyte fuel cell assemblies via X-ray computed tomography, Electrochim. Acta 242 (2017) 125–136.

[24] N. Kardjilov, A. Hilger, I. Manke, Conrad-2: cold neutron tomography and radiography at ber ii (v7), J. Large-Scale Res. Facil. JLSRF 2 (2016) 98.

[25] https://en.wikipedia.org/wiki/Central_limit_theorem.

[26] S.M. Kay, Fundamentals of Statistical Signal Processing, Prentice Hall PTR, 1993.

[27] https://en.wikipedia.org/wiki/Coefficient_of_determination.

[28] A. Iranzo, P. Boillat, Liquid water distribution patterns featuring back-diffusion transport in a PEM fuel cell with neutron imaging, Int. J. Hydrogen Energy 39 (30) (2014) 17240–17245.

[29] A. Iranzo, A. Salva, P. Boillat, J. Biesdorf, E. Tapia, F. Rosa, Water build-up and evolution during the start-up of a PEMFC: visualization by means of Neutron Imaging, Int. J. Hydrogen Energy 42 (19) (2017) 13839–13849.

[30] J.J. Gagliardo, J.P. Owejan, T.A. Trabold, T.W. Tighe, Neutron radiography characterization of an operating proton exchange membrane fuel cell with localized current distribution measurements, Nucl. Instrum. Methods Phys. Res. Sect. A Accel. Spectrom. Detect. Assoc. Equip. 605 (1–2) (2009) 115–118.

[31] H. Murakawa, K. Sugimoto, K. Miyata, H. Asano, N. Takenaka, Y. Saito, Visualization of water behavior in the in-plane and throughplane directions in a PEFC using a neutron image intensifier, Physics Procedia 43 (2013) 277–281.

[32] P. Oberholzer, P. Boillat, R. Siegrist, R. Perego, A. Kästner, E. Lehmann, G.G. Scherer, A. Wokaun, Cold-start of a PEFC visualized with high resolution dynamic in-plane neutron imaging, J. Electrochem. Soc. 159 (2) (2011) B235–B245.

[33] Q. Meyer, S. Ashton, P. Boillat, M. Cochet, E. Engebretsen, D.P. Finegan, X. Lu, J.J. Bailey, N. Mansor, R. Abdulaziz, O.O. Taiwo, Effect of gas diffusion layer properties on water distribution across air-cooled, open-cathode polymer electrolyte fuel cells: a combined ex-situ X-ray tomography and in-operando neutron imaging study, Electrochim. Acta 211 (2016) 478–487.

[34] P. Boillat, Advanced Characterization of Polymer Electrolyte Fuel Cells Using High Resolution Neutron Imaging, Diss. ETH Zurich, 2009.

[35] K. Yoshizawa, K. Ikezoe, Y. Tasaki, D. Kramer, E.H. Lehmann, G.G. Scherer, Analysis of gas diffusion layer and flow-field design in a PEMFC using neutron radiography, J. Electrochem. Soc. 155 (3) (2008) B223–B227.

[36] P.V. Suresh, S. Jayanti, A.P. Deshpande, P. Haridoss, An improved serpentine flow field with enhanced cross-flow for fuel cell applications, Int. J. Hydrogen Energy 36 (10) (2011) 6067–6072.

[37] D. Spernjak, A.K. Prasad, S.G. Advani, Experimental investigation of liquid water formation and transport in a transparent single-serpentine PEM fuel cell, J. Power Sources 170 (2) (2007) 334–344.

[38] M.A. Hickner, N.P. Siegel, K.S. Chen, D.N. McBrayer, D.S. Hussey, D.L. Jacobson, M. Arif, Real-time imaging of liquid water in an operating proton exchange membrane fuel cell, J. Electrochem. Soc. 153 (5) (2006) A902–A908.

[39] J.P. Owejan, T.A. Trabold, D.L. Jacobson, D.R. Baker, D.S. Hussey, M. Arif, In situ investigation of water transport in an operating PEM fuel cell using neutron radiography: Part 2–Transient water accumulation in an interdigitated cathode flow field, Int. J. Heat Mass Tran. 49 (25–26) (2006) 4721–4731.

[40] J.B. Siegel, D.A. McKay, A.G. Stefanopoulou, D.S. Hussey, D.L. Jacobson, Measurement of liquid water accumulation in a PEMFC with dead-ended anode, J. Electrochem. Soc. 155 (11) (2008) B1168–B1178.